Tracking Traveling Ionospheric Disturbances through Doppler-shifted AM radio transmissions

Claire C. Trop[1,2], James LaBelle[2], Philip J. Erickson[3], Shun-Rong Zhang[3], David McGaw[2], Terrence Kovacs[2]

5   [1]Applied Physics Laboratory, Johns Hopkins University, Laurel, MD, USA
[2]Department of Physics and Astronomy, Dartmouth College, Hanover, NH, USA
[3]Haystack Observatory, Massachusetts Institute of Technology, Westford, MA USA

10   *Correspondence to*: Claire C. Trop (Claire.Trop@jhuapl.edu) or James W. LaBelle (james.w.labelle@dartmouth.edu)

Abstract. Six specialized radio receivers were developed to measure the Doppler shift of amplitude modulation (AM) broadcast radio carrier signals due to ionospheric effects. Five were deployed approximately on a circle at a one-hop distance from an 810-kHz clear-channel AM transmitter in Schenectady, New York, and the sixth was located close to the transmitter, providing a reference recording. Clear-channel AM signals from New York City and Connecticut were also received. The experiment confirmed detection of travelling ionospheric disturbances (TIDs) and measurement of their horizontal phase velocities through monitoring variations of the Doppler shift of reflected AM signals imparted by vertical motions of the ionosphere. Comparison of thirteen events with simultaneous global navigation satellite system (GNSS) based TID measurements showed generally good agreement between the two techniques, with differences attributable to differing sensitivities of the techniques to wave altitude and characteristics within a complex wave environment. Detected TIDs had mostly southward phase velocities, and in 4 cases they were associated with auroral disturbances that could plausibly be their sources. A purely automated software technique for event detection and phase velocity measurement was developed and applied to one year of data, revealing . that AM Doppler sounding is much more effective when using transmitter signals in the upper part of the AM band (above 1 MHz) and demonstrating that the AM Doppler technique has promise to scale to large numbers of receivers covering continent-wide spatial scales.

1 Introduction

Travelling Ionospheric Disturbances (TIDs) are a category of ionospheric variations characterized by propagating wavelike undulations in the ionospheric layer height and/or variations in ionospheric electron density. TIDs have been studied since the earliest days of ionospheric radio research [reviews by Hunsucker, 1982; Hocke and Schlegel, 1996]. They are typically classified as: medium scale (MSTIDs), having horizontal wavelengths of hundreds of kilometers, periods of 15-60 minutes, and horizontal phase speeds 250-1000 m/s; and large scale (LSTIDs), having horizontal wavelengths exceeding 1000 km, periods of 30-180 minutes, and horizontal phase speeds of 400-1000 m/s [Hernández-Pajares et al., 2012; Otsuka et al, 2013;

Tsugawa et al., 2004; Ding et al., 2014]. TIDs can be the ionospheric signature of atmospheric processes such as gravity waves [review by Yeh and Liu, 1974; Francis, 1975; Fritts and Alexander, 2003] or can result from electrodynamically driven ionospheric processes such as the Perkins instability [Perkins, 1973; Kelley, 2011; Makela and Otsuka, 2011]. Atmospheric

35 gravity waves associated with TIDs are an important mechanism of energy and momentum transport between atmospheric regions. For example, storm-time LSTIDs involve significant energy transport from high to low latitudes [Richmond, 1978; Yeh and Liu, 1974]. Gravity wave energy altitudinal transport, typically from lower to higher altitudes, has significant effects on atmospheric temperature dynamics, such as determining the seasonal variation of the mesopause temperature minimum [e.g. She et al., 2022] . In addition to these important effects on atmospheric structure and energy/momentum flow, TIDs can

40 significantly affect both trans-ionospheric and sub-ionospheric radiowave propagation, including impacting radio communications systems as discussed by e.g. Frissell et al. [2022].

TIDs have been detected by many remote sensing methods, including ionosondes, optical cameras, GNSS TEC, coherent and incoherent scatter radars, and Doppler sounding using dedicated transmitters. From the earliest investigations, radio methods

45 using transmitters of opportunity have played a significant role. Even before TIDs were first identified, variations in radio reflection height were detected by Essen [1935], using an early installation of US national time station WWV at 5 MHz frequency, and probably represent a TID detection. A host of early studies measured and statistically characterized TIDs with the Doppler sounding method using the regular and highly stable U.S. National timing standard signal WWV broadcast at HF frequencies from Fort Collins, Colorado and received in Palo Alto, California [Chan and Villard, 1962; Davies et al., 1962;

50 Fenwick and Villard, 1960; Sears, 1972]. Similar studies at HF frequencies exploited the Canadian timing signal CHU [Toman, 1975], an Australian telecommunications timing signal [Joyner and Butcher, 1980], and the Russian timing signal RWM [Reznychenko et al. 2020]. Tedd et al. [1984] observed one-hour timescale, ~5 degree variations in bearing deflections on 600-1000 km paths from transmitters of opportunity in central Europe, which matched TID-based modelling. In the 1980's, several groups collaborated to measure the Japanese standard timing signal JYY on 8 MHz at multiple receivers, determining the

55 horizontal wavelength for different frequencies in the TIDs and combining these to determine a dispersion relation which matches the theoretical prediction for waves just below the Brunt-Vaisäla frequency [Shibata et al. 1983; Tsuitsui et al., 1984]. Tanaka et al. [1984] used Doppler sounding of the JYY timing signal at multiple sites to investigate a mechanism of TID generation by a 1982 earthquake.

60 Probably the most sophisticated application of transmitters of opportunity to measure TIDs is Frequency Angular Sounding (FAS), whereby time series variations of Doppler shift, elevation of arrival, and azimuth of arrival can be inverted with certain assumptions to reconstruct the shape of the causative corrugations on the underside of the ionosphere and their time variations. Applying this technique to a transmitter of opportunity on a 700-km path using the large antenna array at the Kharkiv radio telescope facility in Ukraine, Beley et al. [1995] obtained a remarkably detailed reconstruction of the underside of the

65 ionosphere (their Figure 7). Subsequent work showed that this method could work successfully with much smaller receiving

systems observing a transmitter of opportunity such as CHU, suggesting that world-wide digisonde networks could be employed to do FAS on a regular basis [Galushko et al., 2003; Paznukhov et al., 2012].

Two recent papers illustrate TID detection using HF and MF transmitters of opportunity not related to national timing signals. Chilcote et al. [2015] showed that observations of ~0.1-Hz Doppler shifts of carrier frequencies of two clear-channel AM radio

70 stations over several hundred kilometer paths at three receiver locations allow detection of TIDs. The study included one event with ~1-hour period simultaneously measured with GNSS TEC, coherent backscatter radar, and a nearby digital ionosonde (digisonde); during the event, a nearly 180-degree discrepancy was observed between the TID horizontal velocity inferred from spaced measurements of AM signals versus that inferred from time history of GNSS TEC maps. Recently, Frissell et al. [2022] showed TID detection and characterization through statistics of large numbers of detected serendipitous links between

75 amateur radio operators.

The work of Chilcote et al. [2015], and in particular the discrepant horizontal phase velocity measurement reported therein, inspires the study presented below. Compared to Chilcote's work, our study employs a larger number of receiver locations distributed more widely around the signal source, and further develops methods of detecting and characterizing TIDs through

80 Doppler sounding of AM radio stations using multiple receiver locations and advanced signal processing techniques. Section 2 describes the instrumentation used in this study and the places where it was deployed. Section 3 describes the methodology of TID detection and horizontal phase velocity determination. Section 4 discusses validation of these measurements using GNSS TEC data, and Section 5 shows evidence for auroral sources of some of the events. Section 6 applies automated data analysis to a large amount of data suggesting how the method can scale up to much larger numbers of receiver

85 locations. Finally, Section 7 summarizes the results and suggests future directions of study.

2. Methodology

90

The TID measurement system in this study consists of several elements: antenna/preamp, GPS antenna/receiver, upconverter, software defined radio, Raspberry-Pi microcomputer, and solid-state disk drives. The antenna is a vertically-oriented square magnetic double loop 45 cm on a side, mounted on a ~4-foot mast. The resulting antenna pattern is a dipole with a null at zero elevation in one direction, with capability of receiving AM signals down to relatively low elevations in

95 almost all directions. An active pre-amplifier mounted on the antenna mast amplifies, band-limits, and buffers the induced signal to transmit it down 100-500 feet of coaxial cable (depending on site). Figure 1a shows the antenna/preamplifier in a typical setting on the roof of an academic building. At the receiver end is a bias-tee allowing pre-amplifier power and RF signal to be sent on the same cable. In the receiver, the signal is upshifted by 129.6 MHz by mixing with a GPS-disciplined

local oscillator signal generated in custom electronics, putting the AM broadcast band in the sampling range of the software

100   defined radio (SDR). The RTL-SDR (using the RealTek chipset) uses a GPS-disciplined local oscillator synthesized in

custom electronics and together with associated processing software running on a Raspberry-Pi microcomputer to record in-

phase and quadrature waveforms corresponding to a 1 MHz bandwidth centered on 1100 kHz, covering most of the AM

band (600-1600 kHz). Data collection runs continuously for 14-19 hours/day, centered on nighttime. Figure 1b shows the

receiver with attached cables and disk drive, and Figure 1c is a block diagram of the receiving system.

105
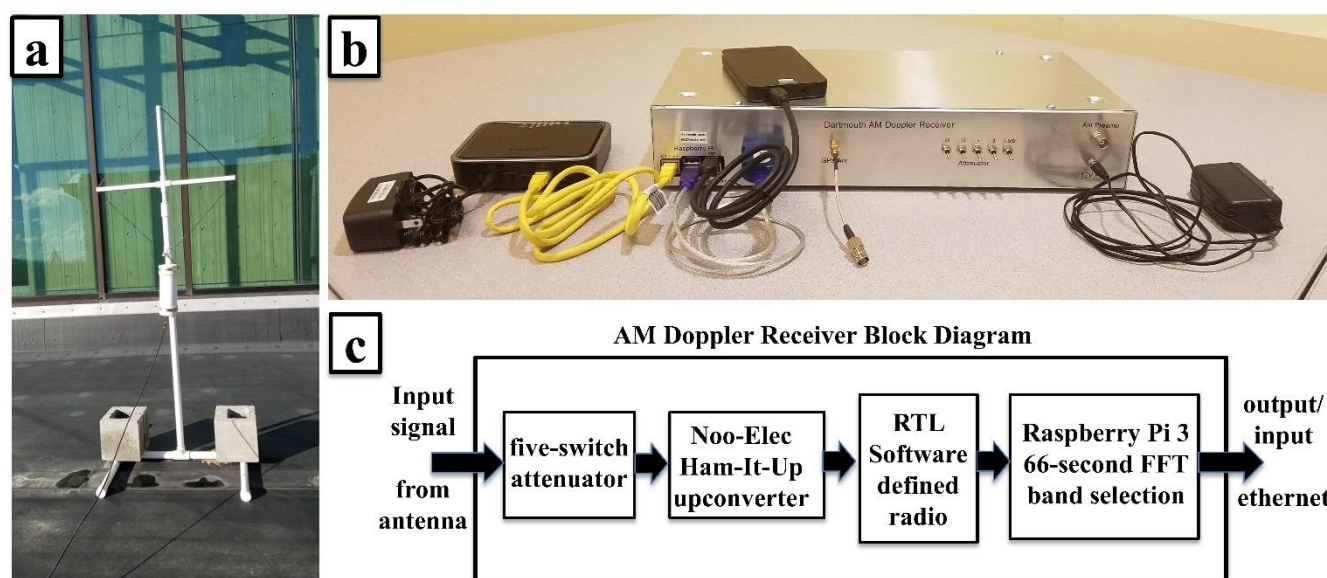
Figure 1: a) The antenna/preamplifier used in the AM Doppler receiving systems, as deployed on the rooftop of an academic

building; b) the AM Doppler receiver with associated cabling and external disk drive; c) a block diagram of receiver.

110   Initial data processing is performed in real time on the Raspberry-Pi. Achieving multiple narrow effective bandwidths for

AM carrier detection from the input continuous I/Q sample stream requires a very long (64M) Fourier transform. To

accomplish this task with limited computer memory, an 8192x8192 array implementation is used which is a variation on

those described extensively in the literature [e.g., Hocking, 1989; Ransom et al., 2002; and references therein]. This

implementation has the advantage not only of limiting memory requirement, but the computation can be limited to the

115   desired frequency resolution. In this case, approximately one hundred 8-Hz bands are used bracketing the frequencies of

each AM signal, which in the US are licensed on 10 kHz spacings within the measured 1-MHz band. The resulting ~100

power spectra have 0.016 Hz frequency resolution and a cadence of 33.5 s. Operation during 12-14 nighttime hours yields

160 MB of compressed data per day. From most sites, the data are transmitted daily to a master server at Dartmouth College,

where custom software produces daily survey spectrograms displaying signal variation on selected AM stations. At sites
120 having limited data transmission, software on the local Raspberry-Pi produces the survey spectrograms which are transmitted
daily as compact PDF files. At those sites, locally stored data are periodically backed up to an external disk drive which is
mailed to Dartmouth.

From April 2020 through March 2021, the hardware and software systems described above were deployed at six locations in
125 the northeastern United States: Hanover, New Hampshire; New Bedford, Massachusetts; Ithaca, Schenectady, and Massena,
New York; and Jenny Jump, New Jersey. Figure 2 shows a map of these locations and Table 1 gives their exact latitudes and
longitudes. The stations are arrayed around a targeted clear-channel and high power (50 kW) AM radio transmitter, 810 kHz
WGY in Schenectady New York, indicated by a black star in Figure 2. Under FCC license regulations, clear-channel AM
radio stations are the only allowed commercial transmission in a given frequency range and in theory should not be subject
130 to interference. Red square symbols in Figure 2 show the nominal reflection locations of the signal paths of WGY to five of
the receivers assuming one-hop propagation. The nominally measured reflection points cover a clock-like pattern spanning
an approximate 200 by 200 km area. Some of the data shown below pertains to additional clear-channel AM stations: 1560
kHz WFME in New York City and 1080 kHz WTIC in Hartford, Connecticut, marked by blue stars. Blue circles in Figure 2
shows the nominal reflection locations of the signal paths of WFME and WTIC to the six receivers, which cover a similar
135 area of approximately 200 by 200 kms each, but offset from that covered by the paths to the primary targeted AM station
WGY. As pointed out by Chilcote et al. [2015], monitoring TIDs via Doppler sounding of clear-channel AM signals requires
placing one receiver next to the target AM transmitter in order to record a reference signal, allowing separation of
ionospheric Doppler shifts from variations in carrier frequency due to imperfect transmission equipment. In the present
experiment, this is achieved with the receiver at Schenectady in the case of receiving WGY, the receiver at Jenny Jump in
140 the case of receiving WTIC, and the receiver at New Bedford in the case of receiving WFME. In practice, only the WGY
signal measured by the receiver in Schenectady required corrections to remove AM transmitter carrier drift.
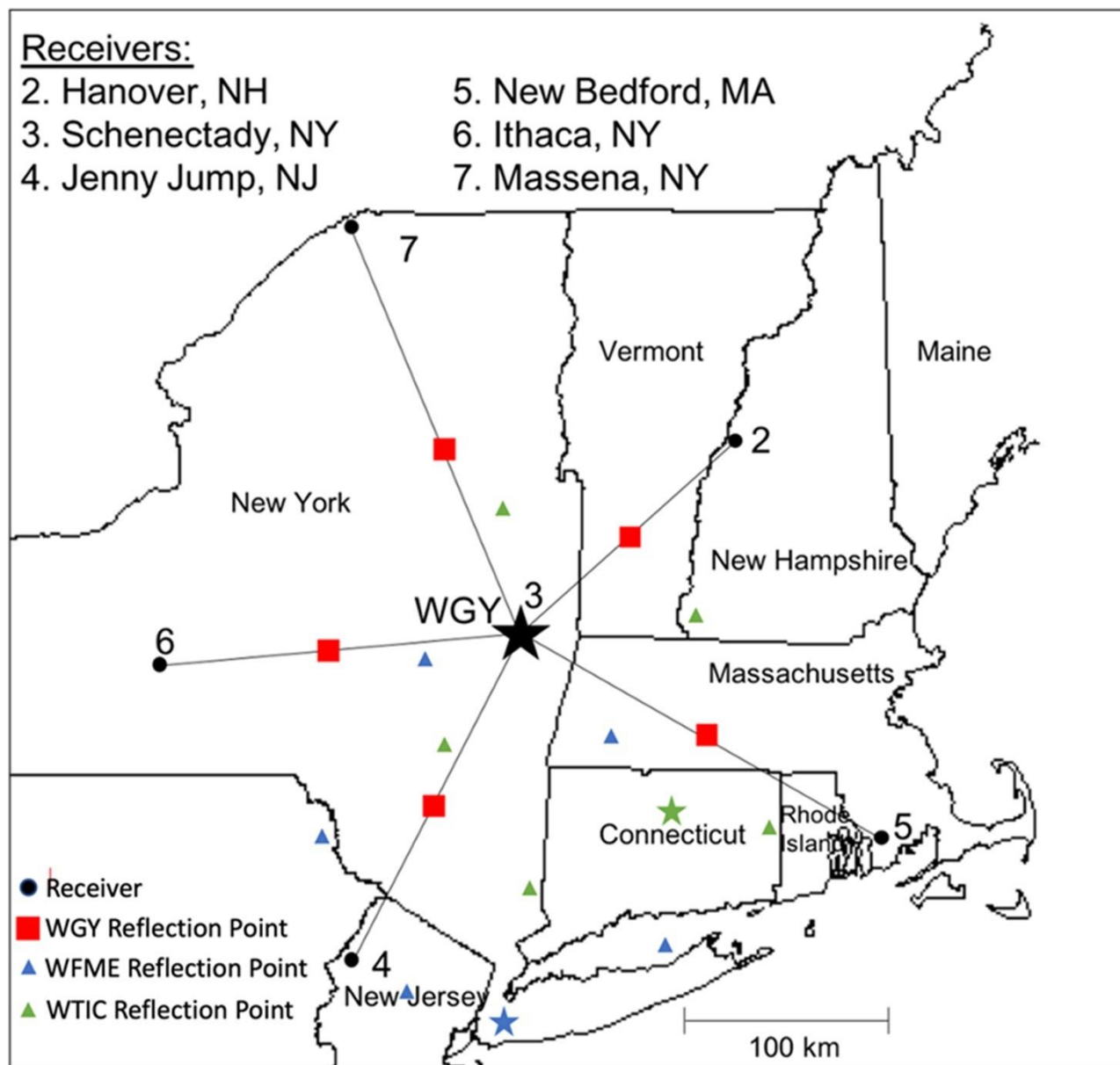
Figure 2: Map showing locations of transmitters (stars) and receivers (circles). Assuming specular, single-hop reflection places reflection points (squares and triangles) at the midway points. The network is designed for reception of the 810 kHz WGY clear-channel AM transmitter out of Schenectady, NY. The receivers encircle the WGY transmitter measuring the reflected wave in all directions over similar path lengths. Additional clear channel signals at 1080 kHz (WTIC) and 1560 kHz (WFME) can be detected by the network, but reflected signals are measured over a limited angular extent across different path lengths.

150   Table 1: Locations of AM Doppler sounder receivers used in this study.

Receiver	Latitude (°N)	Longitude (°E)
Hanover, NH	43.705	-72.286
Schenectady, NY	42.813	-73.912
Jenny Jump, NJ	40.907	-74.925
New Bedford, MA	41,595	-70.910
Ithaca, NY	42.496	-76.431
Massena, NY	44.924	-74.898

155   **3. TID Detection and Phase Velocity Determination**

Figure 3 shows the reflected skywave from the 810 kHz WGY clear-channel station from each receiver from 2100 to 1200 UT on the night of 26 September, 2020. Evidence of a TID passing over the receiver array is apparent in the coherent variations in the signal attributed to the Doppler shift from 0130 to 0400 UTC on all six receivers. The signatures strongly resemble those reported by Chilcote et al. [2015], although their measurement involved only three receivers.

160
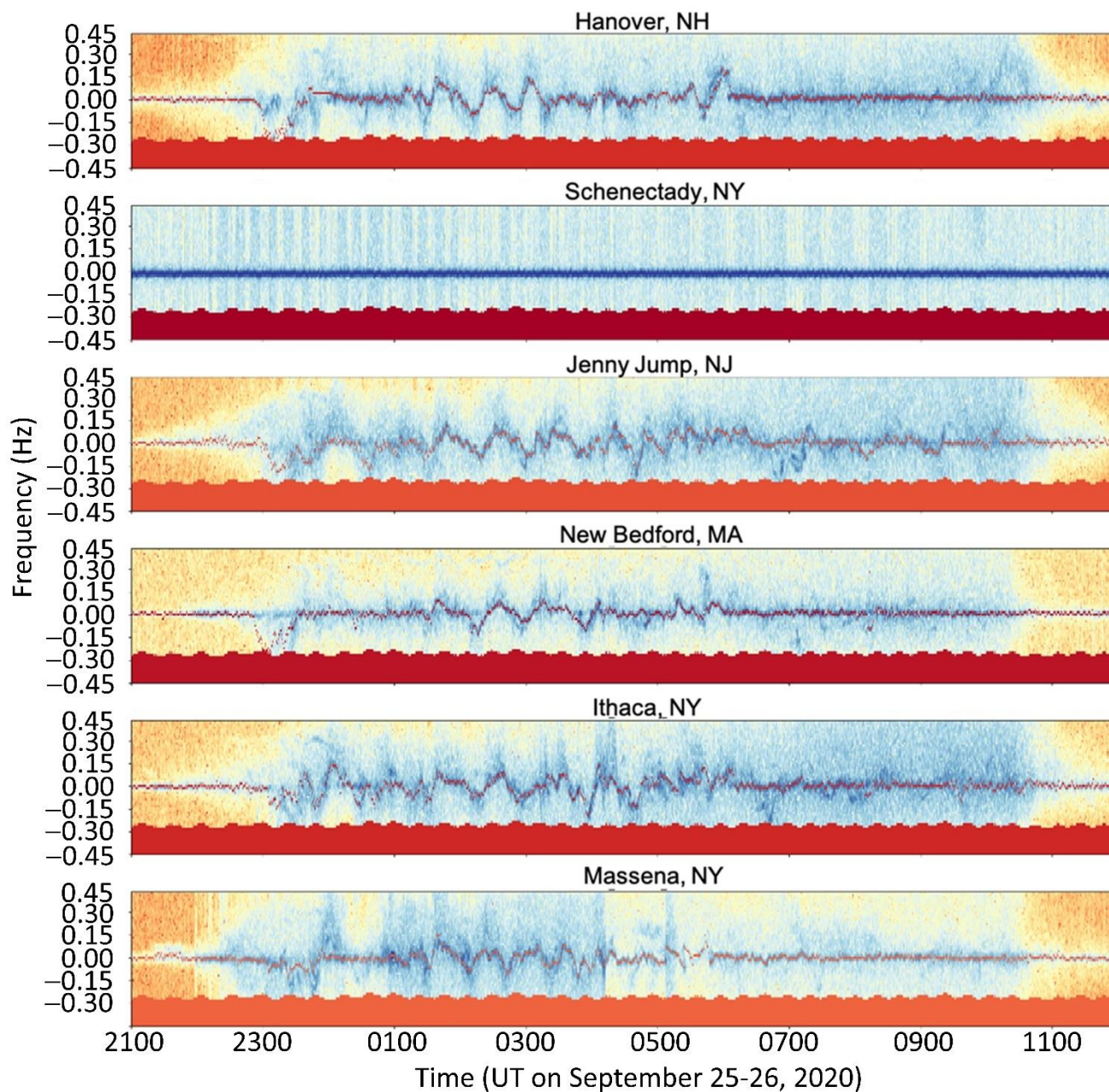
Figure 3: Spectrograms of the 810 kHz signal received at each location in the network covering 0.9 Hz bandwidth from 2200 UT on 25 September to 1200 UTC on 26 September, 2020. The solid colored blocks at the base of each spectrogram illustrate the corrections made to account for variations in the frequency of the transmitted signal. The overlaid (red) trace is the extracted waveform generated by the semi-automated tracking algorithm with manual correction, as described in the text.

The red dashed lines on each receiver in Figure 3 trace the semi-automated tracking of the waveform used for analysis of TID characteristics. The semi-automated tracking searches for maximum excursions from the carrier frequency, assigning these locations as anchors, and then tracks carrier frequency between these points with limits on the step size between
170 adjacent points to ensure continuity. After preliminary tracking by the automated function, manual corrections are incorporated where the automated trace diverged from the skywave. Challenges to the automated tracking include the presence of a high intensity ground wave (for example, see the New Bedford receiver at 0400 UTC), multi-path conditions resulting in multiple Doppler shifted signals at different frequencies (for example, see the Jenny Jump receiver at 0300 UTC), or events when the signal is multi-valued and folds back on itself (third panel of Figure 6 of Chilcote et al. [2015]).
175 The manual correction ensures a consistent carrier trace across all receivers.

A set of traces from a ring of receivers can be used to estimate the horizontal phase velocity of the TIDs detected by the system. The time delay of the variations of the Doppler shifted signals between pairs of stations is the measured quantity used to determine the phase velocity. This time delay is determined using cross correlation between each receiver's signal
180 and the Hanover receiver's signal. A high correlation coefficient identifies maximum similarity between the signals. Using a sliding window, the cross correlation function is executed across the entire domain of traced signals, and time intervals with stationary time delay and a high correlation coefficient are identified as intervals potentially containing TIDs. Stationarity, defined here as a stable delay that does not change with time for an extended period, typically of order one hour, is required to ensure that the disturbance causing the Doppler shifts is consistent in shape and velocity across the entire array. Figure 4
185 shows the stationary, high correlation time delays calculated with respect to the Hanover (light green) receiver for the event on the night of 26 September, 2020 between 0130 and 0200 UTC. From the given time delays, it is immediately evident that the observed TID is propagating in the S/SE direction across the array as indicated by the red arrow.
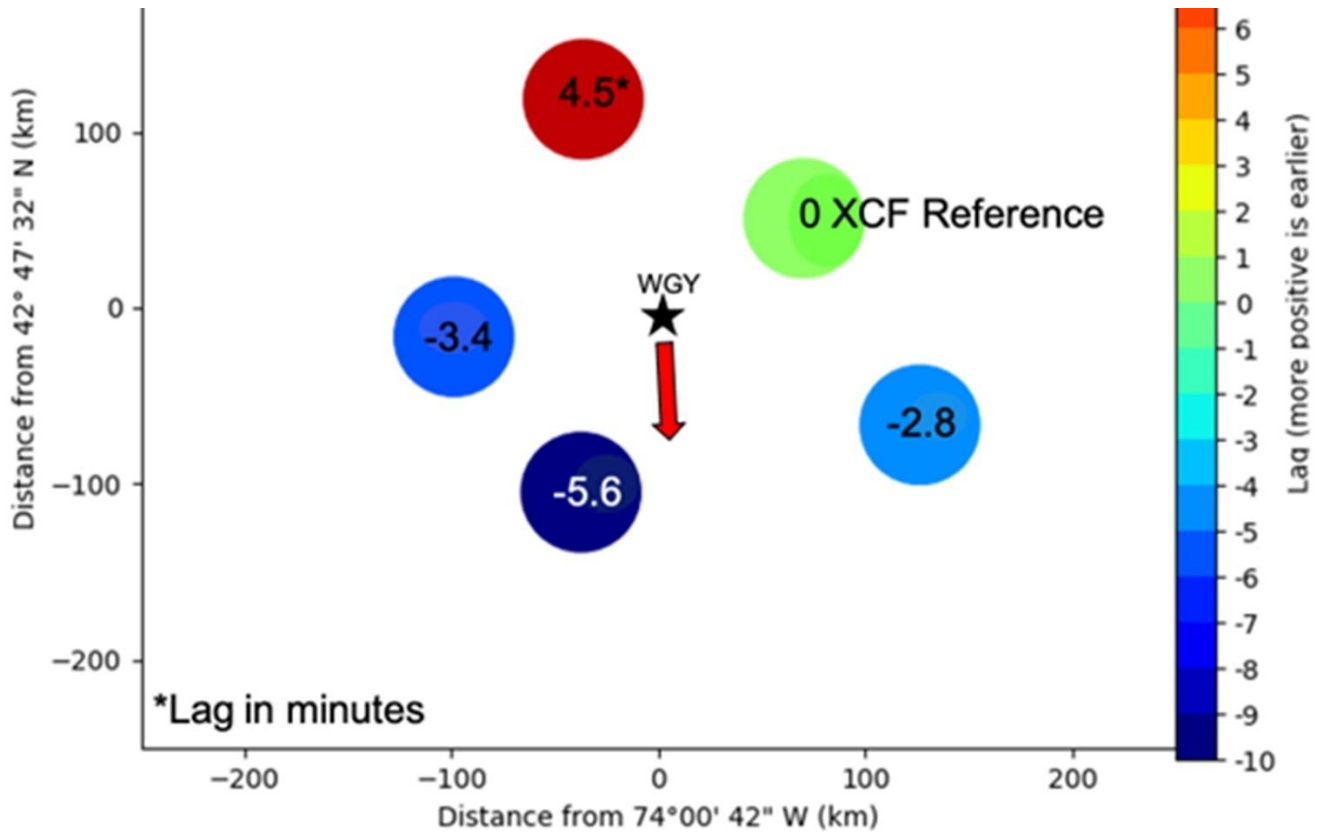
Figure 4: Map showing the location of each reflection point along with the time lag between frequency variations detected at each receiver and those detected at the Hanover, NH receiver (arbitrarily chosen as reference), for the event detected at 0200 UTC on 26 September, 2020. Red colors indicate positive lags (signals arriving earlier), and blue colors indicate negative lags (signals arriving later). The observed lag times indicate a southern direction of propagation (arrow) for the observed TID.

We use three methods for determining the phase velocity from the time delays, denoted as triad, slowness, and sine fit method, respectively. The triad method is a vector geometry approach to phase velocity which can be statistically analyzed because our experiment includes many baselines; i.e. many combinations of receiver triplets. A phase velocity can be calculated for each triplet as follows: for two pairs of receivers composing the triplet, the distance between reflection points is divided by the time delay between the received signals and inverted to get vector components, and adding these vectors provides an estimate of inverse phase velocity pertinent to the triplet. This calculation is repeated for all possible combinations of three receivers and averaged to get a final estimate for the phase velocity:

$$
V_{phase} = \frac{N}{\sum_{n=1}^{N!/_{3!(N-3)!}} \frac{2}{3} * \left[\sum_{i=1}^{3} \sum_{j=i+1}^{3} \frac{\vec{lag}_{ij}}{d_{ij}} \right]} , \tag{1}
$$

The sine method casts the reflection points onto a circle. Each point is assigned an angular value corresponding to its

205 location on the circle (x-value) and a magnitude based on the time delay (y-value). These points are fit with a sine wave. The amplitude of the sine wave coupled with the radius of the circle that defined the positions of the reflection points yields the magnitude of the phase velocity and the phase shift of the sine wave indicates the direction of propagation.

The slowness method for tracking activity captured by a receiver array was originally developed in the seismology

210 community [Lacross et al., 1969] and also applied to location of thunder sources in storms [Johnson et al., 2011]. Chum et al. [2014] and Chum and Podolska [2021] adapted this method for TIDs with a Doppler sounding array. As implemented with our array, the slowness parameter is defined as the inverted phase velocity. Sampling a range of x and y components of the slowness generates an energy map, as defined by Chum et al. [2014], which is a measure of the alignment of the waveforms at the center of the array. The energy map, $W(s_x, s_y)$, is defined by:

215 $$W(s_x, s_y) \propto \sum_{t_i=-\frac{\Delta t}{2}}^{\frac{\Delta t}{2}} \left[\frac{\sum_{n=1}^{N} f_{Dn}(t_i + s_x \Delta x_n + s_y \Delta y_n + s_z \Delta z_n)}{N} \right]^2 ,$$ (2)

and normalized according to:

$$C(s_x, s_y) \propto \frac{W(s_x, s_y)}{\frac{1}{N} * \sum_{n=1}^{N} \left[\sum_{t_i=\frac{\Delta t}{2}}^{\frac{\Delta t}{2}} f_{Dn}(t_i)^2 \right]} ,$$ (3)

where f_{Dn} is the Doppler shift measured at time t_i at the location of each reflection point. The Δx_i values (2) are the distance from each reflection point to the center of the array. Since the array uses only the 810 kHz WGY signal for this study's analysis,

220 the altitudes of reflection are assumed to be equal and the Δz term can be neglected. Figure 5 shows the energy map calculated using the slowness algorithm for 0130-0200 UTC on the night of 26 September, 2020. We define the peak of the energy map (black circle) as the top 97% of values, called slowness correlation coefficients. The distance from the center of the map, calculated with a center of mass calculation over the circled slowness correlation coefficients, is the estimate of the magnitude of the inverse phase velocity, and the azimuthal direction of that center of mass relative to the center of the map is the estimate

225 of the direction of propagation. The upper (lower) bound on the variance of the inverse phase velocity is estimated as the highest (lowest) inverse phase velocity associated with the surface entailing the top 97% of values.
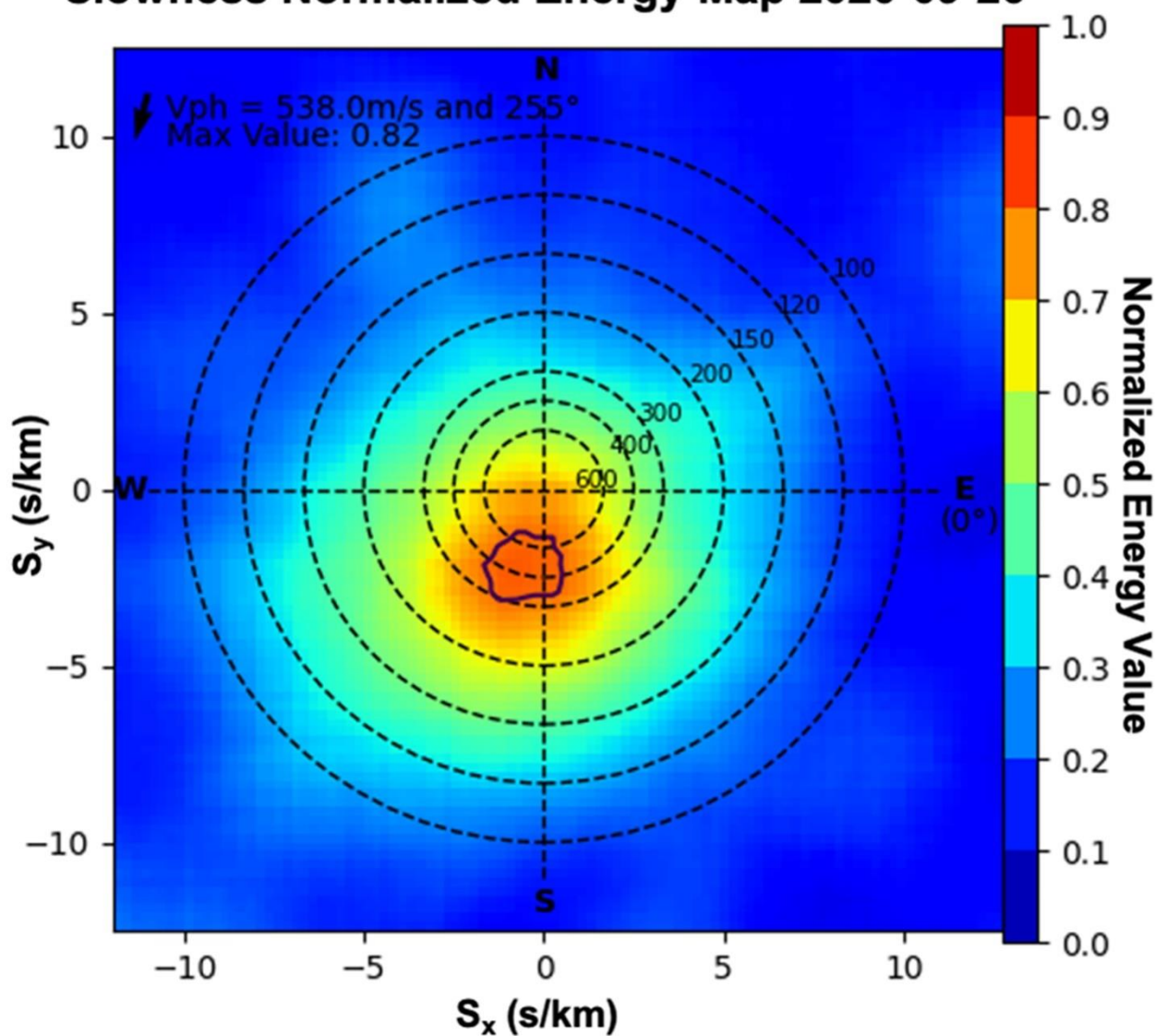
Figure 5: The slowness phase velocity energy map for the event occurring at 0200 UTC on 26 September, 2020. The region outlined with a solid trace indicates the peak region (top 3% of slowness correlation coefficients). The phase velocity magnitude is calculated from a weighted centroid of the energy values within the peak region, and the angle to that centroid indicates the direction of propagation.

Table 2 lists the events detected between 4 February, 2020, and 31 March, 2021, using WGY's 810 kHz station as the

235 transmitter. These events have been initially identified by manual inspection of reflected skywave plots similar to those

shown in Figure 3. The semi-automated tracking described above has been applied to them, and their phase velocities have

been calculated using all three methods. The phase velocities shown in Table 2 are those obtained from the slowness method.

There are seven TIDs detected traveling in the S/SE direction, three events in the SW direction, and two events in the NW

direction. For the event on 10 December, 2020, the slowness method indicates an infinite phase velocity (i.e. the peak

240 correlation coefficients region encircles the origin), although the sine and triad methods imply a southwesterly direction. Of

the thirteen events, four have phase velocities between 100-300 m/s, three between 300-400 m/s, two between 400-500 m/s,

and four above 500 m/s. Larger phase velocities are accompanied by greater uncertainty. The four events below 300 m/s are

likely classifiable as MSTIDs while the remaining eight events above 300 m/s are likely LSTIDs. The median velocity is 347

m/s, the mean velocity was 411 m/s, and the standard deviation is 199 m/s. For reference, the principal TID event analyzed

245 by Chilcote et al. [2015] has a phase velocity of 330 m/s propagating in the northeast direction.

Table 2: List of events detected using WGY Schenectady (810 kHz).

Event Date + Time	Slowness Phase Velocity Magnitude (Direction)	Number of Receivers
2020-03-23: 0400 UTC	$478^{+2277}_{-260}\ m/s$ (S)	3
2020-05-06: 0400 UTC	$673^{+770}_{-373}\ m/s$ (SE)	4
2020-07-14: 0530 UTC	$358^{+88}_{-124}\ m/s$ (SSE)	5
2020-09-09: 0400 UTC	$150^{+26}_{-8}\ m/s$ (NW)	5
2020-09-22: 0500 UTC	$267^{+126}_{-85}\ m/s$ (SE)	4
2020-09-26: 0200 UTC	$538^{+218}_{-244}\ m/s$ (S)	5
2020-09-27: 0400 UTC	$335^{+66}_{-97}\ m/s$ (SE)	5
2020-09-29: 0200 UTC	$859^{+218}_{-425}\ m/s$ (SW)	5
2020-11-15: 0730 UTC	$332^{+107}_{-84}\ m/s$ (SW)	5
2020-12-10: 0700 UTC	n/a	5
2020-12-29: 0700 UTC	$229^{+119}_{-34}\ m/s$ (NW)	4
2020-12-30: 0700 UTC	$418^{+168}_{-155}\ m/s$ (SW)	5
2021-01-26: 0230 UTC	$299^{+192}_{-112}\ m/s$ (S)	5

.

250

The horizontal phase velocities tabulated in Table 2 are those determined from the slowness method. Velocities determined from the sine and triad method methods generally agree with those from the slowness method to within 45 degrees with one (triad) to two (sine) outliers within 90° for the direction of propagation. The triad has a median of 343 m/s, mean of 394 m/s, and standard deviation of 232 m/s. The sine has a median of 298 m/s, mean of 361 m/s, and standard deviation of 258 m/s, but is only functional when all five receivers were operational (9 out of 13 events).

4. Validation with GNSS Technique

For validation beyond the AM network observations, detected TID events can be compared with simultaneous observations of TID characteristics obtained from global navigation satellite system (GNSS) total electron content (TEC) data. TEC is the integrated electron density along a path between a ground receiver and a satellite. Time delays between different frequencies along the same path allow TEC to be calculated (Cooper et al., 2019). The measured TEC quantity is then projected geometrically onto the vertical axis and detrended from the baseline electron content. Detrended TEC as a function of time and space can show periodic increases and decreases which are linked to TID activity (Tsugawa et al., 2007, Zhang et al., 2022). The TEC technique and the AM doppler sounding technique have different sensitivities in wave altitude and wave characteristics.

The detrended TEC (or differential TEC, dTEC) data, plotted in keogram form, is generated using global GNSS observations processed by MIT Haystack Observatory as part of operations for the Millstone Hill Geospace Facility (e.g. Zhang et al., 2017; Zhang et al., 2018). In this analysis, a 30-min sliding window is used to determine the baseline electron content The resulting keograms are analogous to slit cameras. A range of latitudes or longitudes (y-axis) is chosen and the dTEC for that narrow range is calculated and plotted for a number of hours (x-axis). The TIDs become visible on the keograms as coherent regions of periodic increases and decreases in TEC which advance along the diagonal (changing latitude or longitude with time). GNSS data have been analyzed for the time intervals of the TIDs detected by the AM Doppler receivers (listed in Table 2). Figure 6 shows the 35 to 55°N latitude keogram along the selected slit from -75 to -70°E longitude, for the TID event on 26 September, 2020. From the angle of the coherent wave structure, the calculated phase velocity propagated southward at 430 m/s around 0200 UTC. This phase velocity from GNSS TEC agrees well in magnitude and direction with that determined by the AM Doppler receiver network on the same data and time (see Table 2).
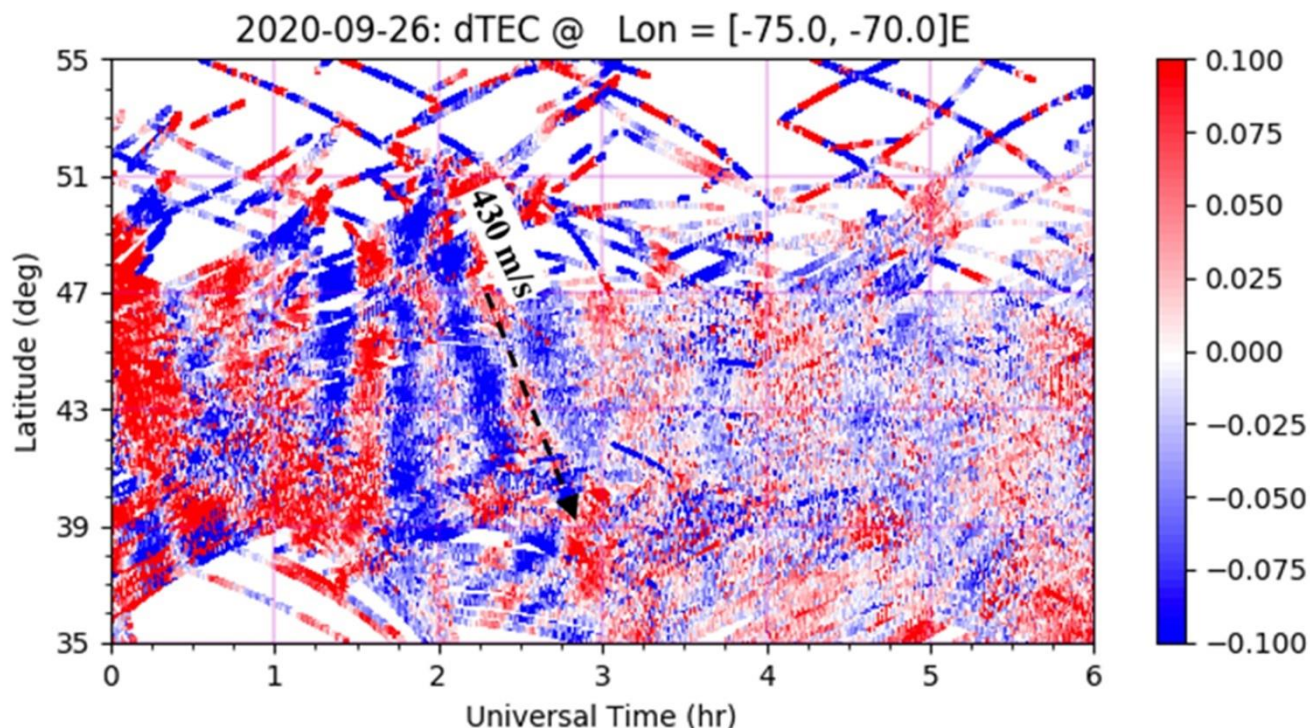
280

Figure 6: Differential TEC keogram for a TID detected via GNSS on the night of September 26th, 2020. The keogram indicates a coherent structure propagating southward with a phase velocity of 430 m/s. The keogram corroborates the TID event direction and speed measured with the AM Doppler receiving network at the same time.

285

Table 3 presents results of comparing each event identified by AM Doppler sounding with simultaneous keograms from GNSS-TEC data. For nine out of the eleven events in which a coherent TID signature was observed in the GNSS-TEC data, the directions of propagation determined from the GNSS-TEC method are within 45 degrees of those determined from the

290 AM Doppler receiver network/slowness analysis. In the four cases for which the GNSS-TEC method indicates only a meridional or zonal component, three of these are within twenty percent of the phase velocities determined from the AM Doppler receiver network/slowness analysis. For the other five events, the GNSS-TEC method indicates both meridional and zonal components. Since phase velocities must be inverted to be added, the smaller amplitude component becomes the dominant phase velocity. In these five cases, the slowness calculated phase velocity is larger than that inferred from the

295 GNSS-TEC method. In fact, out of the eleven events for which the directions agree between the two techniques, nine had slowness phase velocities greater than their TEC counterparts.

Table 3: Comparisons of TID events detected with both AM Doppler sounding and GNSS.

Event Date + Time	Slowness Phase Velocity Magnitude (Direction)	GNSS TEC Phase Velocity Magnitude (Direction)
2020-03-23: 0400 UTC	478 m/s (S)	485 m/s (S)
2020-05-06: 0400 UTC	673 m/s (SE)	320 m/s (S) and 190 m/s (E)
2020-07-14: 0530 UTC	358 m/s (SSE)	645 m/s (S) and 165 m/s (E)
2020-09-09: 0400 UTC	150 m/s (NW)	170 m/s (N) 150 m/s (W)
2020-09-22: 0500 UTC	267 m/s (SE)	154m/s (N) 155 m/s (W)
2020-09-26: 0200 UTC	538 m/s (S)	430 m/s (S)
2020-09-27: 0400 UTC	335 m/s (SE)	140 m/s (W) [well-defined], 115m/s (S) [faint]
2020-09-29: 0200 UTC	859 m/s (SW)	580 m/s (S); 645 m/s (S) LSTID
2020-11-15: 0730 UTC	332 m/s (SW)	130 m/s (N); 165 m/s (W)
2020-12-10: 0700 UTC	n/a	80 m/s (S) and 60 m/s (W) (multiple wavefronts)
2020-12-29: 0700 UTC	229 m/s (NW)	215 m/s (S) and 60 m/s (W); northward components existed but weak
2020-12-30: 0700 UTC	418 m/s (SW)	145 m/s (N) and 80 m/s (W) (multiple wavefronts)
2021-01-26: 0230 UTC	299 m/s (S)	130 m/s (W) (multiple waves)

300

A possible explanation for this observed discrepancy is that the GNSS-TEC method, relying on an integral of electron density through the ionosphere, is most sensitive in general to the peak electron density regions at higher F2 altitudes in the

305 ionosphere, while the AM Doppler sounding technique exclusively looks at reflection off the bottom of the ionosphere. Since a TID has a vertical wavenumber, its characteristics are altitude dependent. The Doppler sounding technique is only able to determine information about the horizontal wavenumber, but contributions from the vertical may be sufficient to explain the discrepancy in magnitude between the two techniques. Another potential factor to consider is the detrending

technique employed in GNSS TID analysis, which may lead to the detection of only specific components of multifrequency
310 waves. In the context of the 30-minute sliding window utilized in this study, larger scale and longer periodicity waves have a
tendency to be attenuated. Table 3 appears to indicate that these GNSS-TEC derived TID phase speeds are indeed slower,
and therefore these waves likely contain some MSTID components.

For two events, the two techniques indicate different directions of propagation. For the first event on 26 January, 2021, the
315 AM Doppler system detects a TID which propagates southward with a phase velocity 219 m/s and has been linked to an
auroral source (see Section 5). However, the TEC keogram detects an event propagating westward with a phase velocity of
130 m/s. It is likely in this case that the two techniques detect two distinct TIDs, one caused by an auroral event and
prominent at lower altitudes and one potentially caused by the electrodynamically driven Perkins instability (Perkins, 1973;
Narayan et al., 2018). The configuration is suggested by the TID's direction of propagation and phase speed which would
320 have more prominent effect at the higher altitudes to which the GNSS TEC technique is more sensitive. For the second event
on 15 November, 2020, the AM Doppler systemdetects a TID propagating southwestward with a phase velocity of 332 m/s
while the GNSS-TEC keogram detects an event propagating northward with a phase velocity of 130 m/s. In the AM Doppler
data, the correlation coefficients for the sliding normalized cross correlation were high and the time delay was stationary,
making it unlikely that error in AM Doppler network/slowness analysis occurred. However, the differences in sensitivities
325 (in wave altitude domain and wave characteristics) of the two techniques could explain the discrepancy. Finally, there are
two events (denoted by n/a in the GNSS0-TEC column of Table 3) detected by the AM Doppler system which are not visible
in the corresponding GNSS-TEC keograms. This difference may also be attributed to the different sensitivities of the two
techniques (to altitude-variable and wave characteristics) TID effects and, coupled with the two events which disagree,
suggests that the AM Doppler technique detect a subset of events which the GNSS-TEC technique does not reveal.
330

In aggregate, the TEC and AM Doppler observations show that the TID wave environment is sometimes complex, with
multiple waves of different characteristics simultaneously present and detected favorably by one technique or the other. The
consistency of the direction between the two techniques for the majority of the observed events in this work suggests that the
unexplained discrepancy between directions of propagation previously seen in Chilcote et al. [2015] was either an outlier
335 event comprising a complex wave environment, similar to the 15 November, 2020, and 26 January, 2021, events in this
study, or due to error introduced by their experimental set up which relied on multiple frequencies from different radio
transmitters and only used three receivers.

340

5. Connections to Auroral Activity

Auroral geomagnetic storms and substorms can enhance the auroral electrojet, which then initiates TIDs through Lorentz forces and Joule heating (Ding et al., 2008). To detect the occurrence of this mechanism, electrojet enhancements can be tracked through the Auroral Electrojet (AE) Index (Davis and Sugiura, 1966) and spatially and temporally isolated using

345 magnetometer data from instruments maintained in several arrays of arctic observatories, such as the Canadian Array for Realtime Investigations of Magnetic Activity (CARISMA), the Canadian High Arctic Ionospheric Network (CHAIN), and the Time History of Events and Macroscale Interactions during Substorms (THEMIS) ground array. Enhancement events can then be correlated with southward propagating TIDs measured across the AM Doppler sounding network in the northeast United States.

350

Figure 7 shows the AE electrojet index for 0000-1200 UTC on 14 July, 2020, and a map of magnetometer activity at 0330 UTC on the same date. An enhancement in AE occurs at approximately 0340 UTC, 1:50 prior to a southeastward propagating TID with a measured phase velocity of 358 m/s on 14 July, 2020 (Table 2). Assuming that the group and phase velocities are on the same order, the distance traveled by the TID over the 1:50 between the AE enhancement and its arrival

355 at the AM receiver network is approximately 2360 km. The distance from epicenter of the magnetic activity (Churchill, Manitoba) to the center of our network (Schenectady, NY) is 2300 km, qualitatively confirming the hypothesis that auroral activity and the southward TIDs are correlated in this case. Similar spatial and temporal correlations between enhancements in AE and TID detections with the AM Doppler network are observed on 6 May, 26 September, and 27 September, 2020.
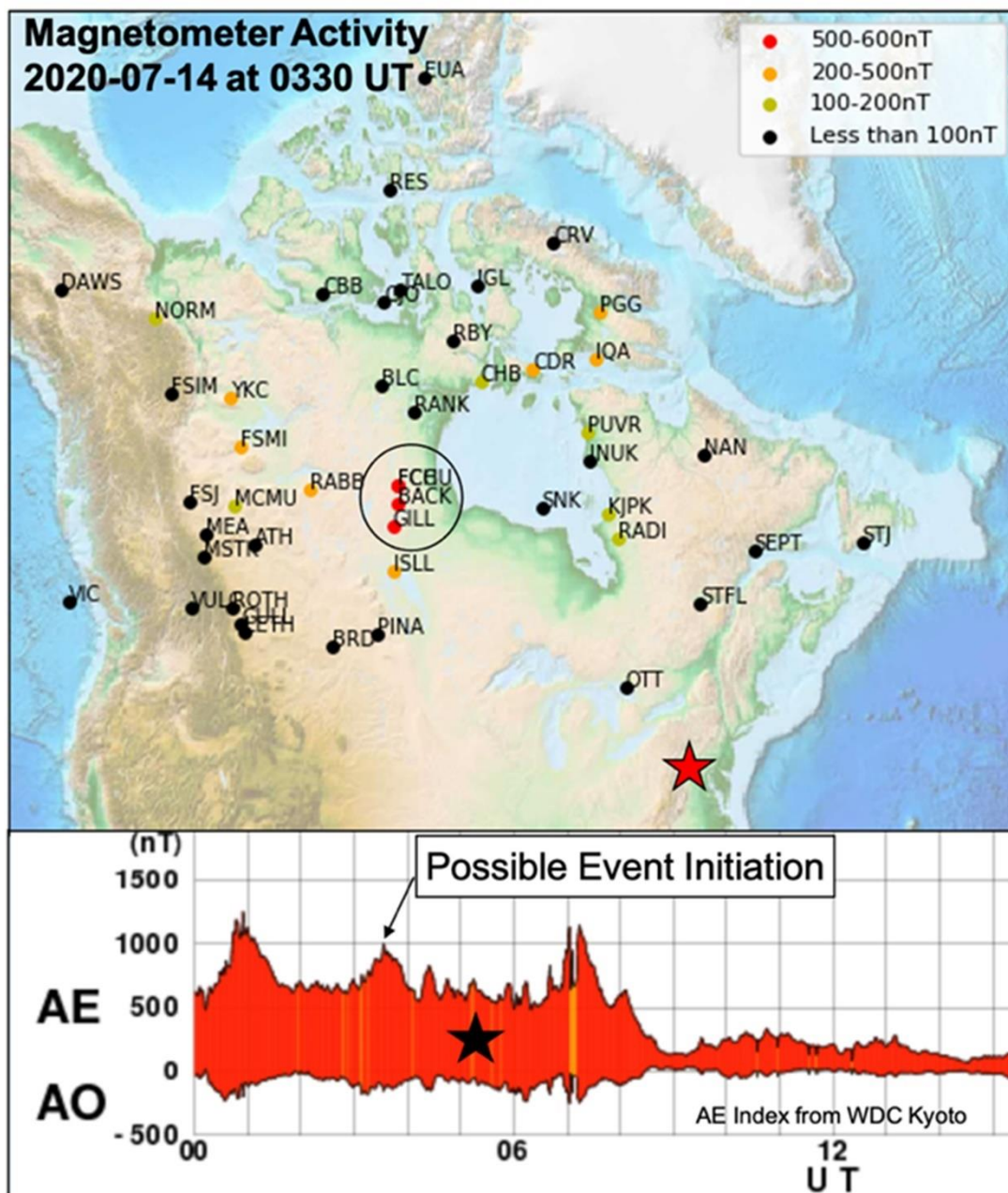
Figure 7: Magnetometer activity (top panel) at 0330 UTC and Auroral Electrojet AE index (bottom panel) for 0000-1500 UTC on 14 July, 2020. at 0330 UTC. The enhancement in AE index at approximately 0340 UTC corresponds to maximum magnetic activity, on the order of 500-600 nT magnitude, in the vicinity of Churchill, Manitoba. This activity precedes a TID event detected with the AM Doppler receiver network in the Northeast United States by 1:50, approximately matching the time it would take a TID with measured the phase velocity of 358 m/s to propagate from Churchill to the measurement array.

6. Fully-Automated Detection and Characterization of TIDs

The results of Sections 3-5 are based on semi-automatic tracking of variations in Doppler shift on six receivers, supplemented by manual corrections. To enable an operational system that considers larger numbers of events and, more importantly, larger numbers of receivers monitoring larger numbers of clear-channel AM stations, it is essential to remove any manual actions and entirely automate event detection and characterization. To test the efficacy of purely automated analysis, a modified version of the tracking software described in Section 3 was applied to a 12-month data set with automated initial peak selection and no manual correction.

Using the resulting Doppler shift versus time on all six receivers tracked fully autonomously, slowness distribution functions were calculated for consecutive 55-minute intervals between sunrise and sunset each day. Intervals for which the maximum slowness correlation value was above an experimentally determined threshold, together with preceding and following intervals, were re-analyzed with higher effective time resolution to determine the interval of maximum correlation between the six receivers. The phase velocity and direction were calculated for these maximum correlation intervals. Events with multi-modal distribution functions or too-large uncertainties in velocity magnitude or direction were discarded.

The auto-tracker method was applied to Doppler sounding data from all receiving sites for the three selected clear-channel AM transmitters for 359 days between 3 April, 2020, and 31 March, 2021. The selected stations were 810 kHz (WGY from Schenectady, New York), 1080 kHz (WTIC from Hartford, Connecticut), and 1560 kHz (WFME from New York City) as shown in Figure 2. The 810 kHz station contained many false positives caused by erroneous slowness correlation coefficients due to the reduced amplitude of the Doppler signatures on WGY, as the lowest frequency station. The false positives were mitigated with a threshold RMS value on the correlation, but event detection still required manual verification.

Figure 8 shows the results of the automated event detection. Each triplet of panels represents the set of events detected with a unique transmitting frequency: 810 kHz (top), 1080 kHz (middle), and 1560 kHz (bottom). Within each set, the top two panels show the events as a function of time of day and time of year. For the top two panels in each set, the color bar at right indicates the magnitude of the phase velocity of each TID. In the second panel, arrows indicate the direction of propagation. In the bottom panel, events are binned by month in histogram format.
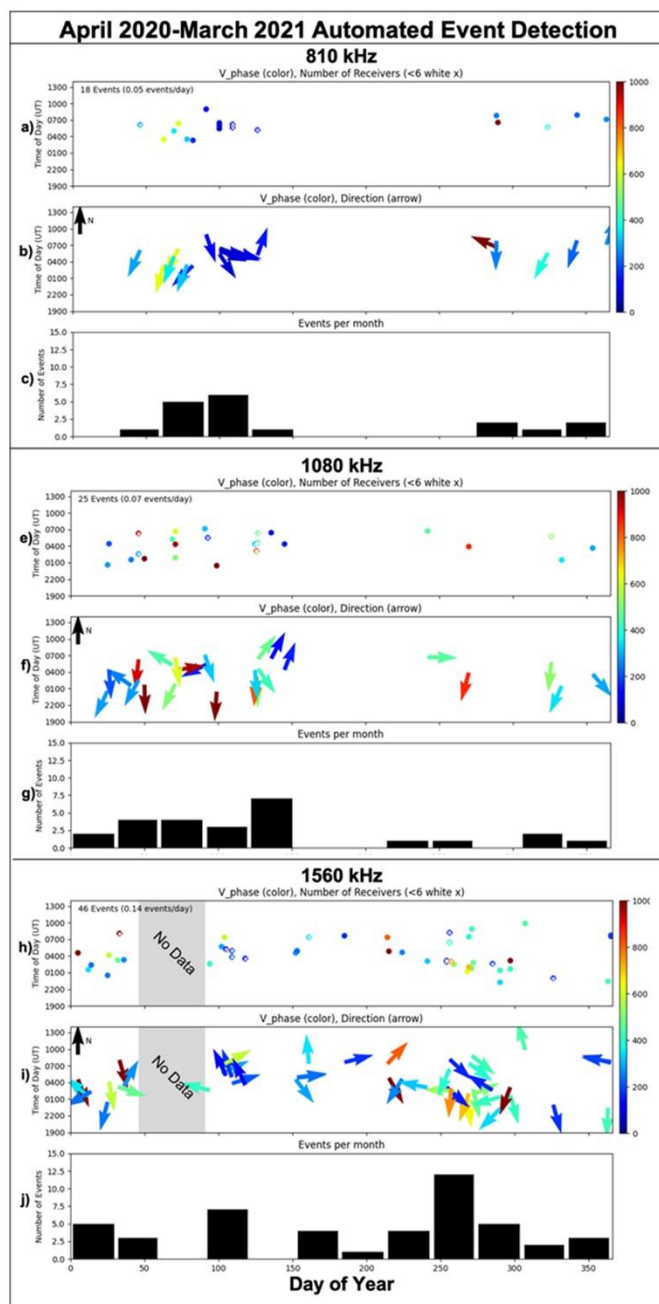
Figure 8: Results of the fully automated tracking and event detection software: Each triplet of panels indicates automatically detected events from 810, 1080, and 1560 kHz AM stations respectively. The top panel of each triplet displays the phase velocity (color) as a function of day of year (x-axis) and time of day (y-axis). The second panel displays the direction of

400 propagation for each event, and the lowest panel groups the detected events by month. Seasonal dependence of maximal event detection suggests the automated tracking favors the detection of LSTIDs (see text discussion).

The method identified 18 TID events on 810 kHz (0.05 events/day), 25 events on 1080 kHz (0.07 events/day), and 46 events
405   on 1560 kHz (0.14 events/day). Significantly, nearly three times the number of events are seen on the highest frequency
station compared to the lowest. Manual inspection of the Doppler spectrograms confirms that the variations in the skywave
traces are much more distinct and auto-tracking more effective for transmitter higher frequencies > 1 MHz, particularly the
variations typical of TIDs. Figure 9 illustrates this difference for an typical TID event observed on 27 September, 2020. The
amplitude of the Doppler shift induced when the AM carrier reflects from a vertically moving ionospheric layer is
410   proportional to the frequency of the signal:

$$\Delta f = -2f * \frac{v}{c} \ , \tag{4}$$

where v is the vertical component of the velocity of the ionosphere, Δf is the frequency excursion, and f is the carrier
415   frequency. Hence, for given TID parameters, the key measured quantity Δf is proportional to the frequency. Furthermore,
higher frequencies reflect at higher altitudes where TIDs themselves have greater amplitudes due to energy conversion as the
number of neutral particles decreases with altitude (Houghton, 1986). In addition to reduced amplitudes, at lower frequencies
it is more common that the radius curvature of the wave is smaller than the mean height. In these case, multiple reflections
can occur for the same frequency, and this generates S-shaped features that fold back on themselves (Fišer et al., 2017).
420   Given that the same ionospheric velocities produce larger absolute deviations from the carrier frequency and are less likely
to exhibit anomalous features, it is therefore not surprising, as Figure 8 confirms, that the AM Doppler technique for
detecting TIDs is much more effective if applied to AM signals in the upper half of the AM frequency band > 1 MHz.
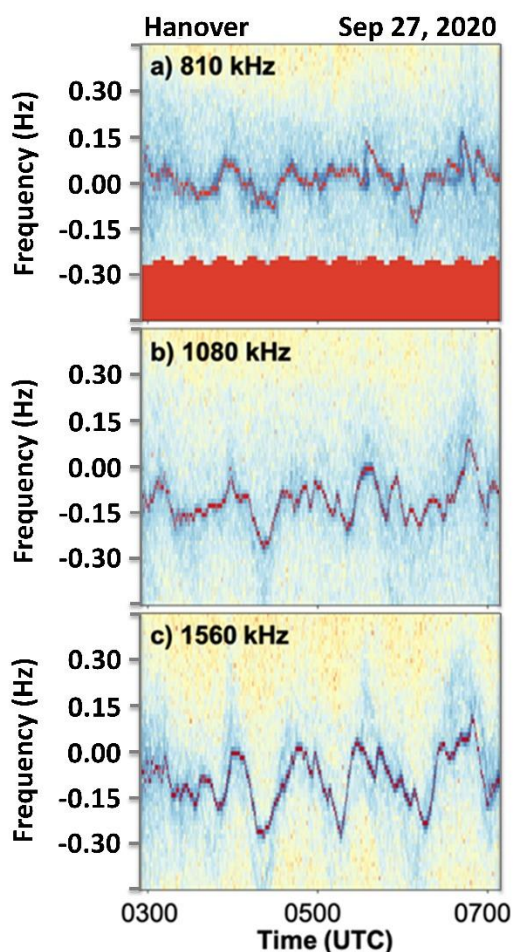
Figure 9: Spectrograms of the 810 kHz, 1080 kHz, and 1560 kHz signals, covering 0.9 Hz bandwidth for 0300-0700 UTC on 27 September, 2020. As expected from equation (4), the Doppler shift is a function of the frequency (larger for higher frequencies). The figure indicates that TIDs may be easier to detect and track using carriers in the upper half of the AM band.

7. Seasonal dependence of AM network identified TIDs and comments on technique optimization

Seasonal dependence of AM network identified TID events are shown in the histogram panels of Figure 8. For all three frequencies, there is a distinct minimum occurrence in the summer (days 150-215). The 1560 kHz station data show a hint of equinoctial peaks. Tsugawa et al. [2004] observed peaks in LSTID occurrence around the equinoxes in the spring and fall, absence of quiet-time LSTIDs in summer, and minimum occurrence of LSTIDs in summer during active geomagnetic periods. Yakovets et al. [2011] and Ding et al. [2014] detected similar activity peaks at the equinoxes for LSTIDs. In

435   contrast, studies tend to report peaks in MSTID activity (especially at night) in the summer and winter [Shiokawa et al.,

2003; Martinis et al., 2010, Otsuka et al., 2013]. Because seasonal statistics of TID characteristics may depend on local time

and region, it is difficult to draw firm conclusions, but the seasonal dependence seen in Figure 8 suggests that the automated

tracking and event detection algorithm employed here may preferentially detect LSTIDs, perhaps because their larger

wavelengths imply that the resulting Doppler shift variation have longer time scales and are easier to track.

440

For all three transmitter frequencies, the detected TIDs primarily propagate southward. Southward components to the phase

velocity are observed for 15 of 18 events on 810 kHz, 19 of 25 on 1080 kHz, and 28 of 46 on 1560 kHz. The east-west

propagation is split almost equally in all three datasets—9 out of 18 westward on 810 kHz, 12 out of 25 westward on 1080

kHz, and 22 out of 46 westward on 1560 kHz. On the 810 kHz station, the phase velocities range from 71 to 1308 m/s with a

445   mean phase velocity of 304 m/s and a standard deviation of 295 m/s. On the 1080 kHz station, the phase velocities range

from 130 to 1453 m/s with a mean phase velocity of 515 m/s and a standard deviation of 329 m/s. On the 1560 kHz station,

the phase velocities range from 104 to 1914 m/s with a mean phase velocity of 445 m/s and a standard deviation of 367 m/s.

Of the 13 events identified for analysis by the manual methods, seven of those events are detected by the auto-tracker on at

450   least one transmitter frequency. The auto-tracker initially detects an additional 2 of the 13 manually detected events, but

these two fail to meet the auto-tracker's criteria on the uncertainty in phase velocity magnitude or direction. The imperfect

overlap between the manually selected events and those detected with the auto-tracker technique may be attributed to the

preferential detection of LSTIDs, the fact that the automated system performs less optimally on the 810 kHz, and the

discrepancies that exist between the two frequencies with purely human-in-the-loop detection and tracking.

455

To investigate discrepancies between the 1560 kHz and the 810 kHz results, the semi-automated analysis described in

Section 3 was applied to the 1560 kHz data set for the thirteen TID events for which a similar analysis applied to the 810

kHz data set is summarized in Table 2. In eight out of ten events for which comparison was possible, the direction of

propagation of the detected TIDs on the 810 vs 1560 kHz matches within 45°, but the magnitude of the phase velocity on the

460   1560 kHz station is generally greater than that measured on the 810 kHz station. This discrepancy could be introduced by

different reflection heights between the two frequencies, or alternatively it could be due to error introduced because the

receivers do not encircle the 1560 kHz station. Therefore, the received signals may be from oblique reflections off the

ionosphere, may have different reflection path lengths, and/or may sample a smaller angular spread of the ionosphere. For

optimal system designs, receivers should encircle the transmitters equidistant from primary transmitters.

465

Ultimately, the results of Figure 8 demonstrate the feasibility of automatic TID detection applied to spectral data of Doppler

shifts of multiple receiver clear-channel AM signals at multiple receiver locations. The results also indicate this technique is

far more effective when applied to signals in the upper part of the AM band. For such signals, the detection software used here

has identified approximately one event per week and seasonal statistics suggest the LSTIDs are favored over MSTIDs. Further
470   refinement of the algorithm could result in sensitivity to more events and greater sensitivity to MSTIDs. The automatic event
detection demonstrated herein is essential if the technique is to be practical using configurations with large numbers of AM
signals measured at a large number of receiving stations.

8. Conclusions

475   This study has demonstrated the efficacy of using a circular network of AM receivers around a single transmitting frequency
to identify TIDs and their characteristics from Doppler shifted reflected skywaves. While Chilcote et al. [2015] showed that
TIDs can be detected via Doppler sounding using AM signals, their use of only three receivers and a number of different
frequencies for a single detected TID did not establish that TID horizontal phase velocity magnitude and direction could be
reliably corroborated by other methods, namely GNSS TEC observations. However, a larger sample set with a more robust
480   measurement design from the present study has shown good agreement—nine out of eleven—with GNSS TEC derived TID
event information. Differences between these two data sets can be attributed to the different sensitivities of the two
measurement techniques in a complex TID wave environment. Most detected TIDs had a southward phase velocity and in four
cases, they were associated with enhanced auroral magnetic activity which may have been their initiation.

485   This experiment, particularly successful implementation of purely automated analysis, clearly indicates that it is possible to
extend AM Doppler sounding to large numbers of receivers. Based on these results, a future experiment could be envisioned
using a few dozen receivers arrayed around a dozen or more clear channel AM transmitters to achieve continental-scale spatial
coverage, allowing TIDs to be tracked for ~1000 km or more. Such an array would effectively complement spatial coverage
of the GNSS technique, allowing differences and similarities between the two techniques to be better understood, to the
490   improvement of both. An array covering continental or half-continental scale would also supplement existing optical,
digisonde, and SuperDARN radar techniques, further leveraging investments and science yield from those already productive
assets. We suggest that future AM Doppler network experiments should employ transmitters in the upper part of the AM band
for best results. Additional refinement of the purely automated algorithm may lead to greater sensitivity and more event
detections.

495   **Data Availability**

Data used in this study are available through LaBelle [2024].

500

Author Contribution

CCT performed most of the data analysis and wrote the initial draft of the manuscript with contributions from the other co-authors. JL participated in deploying the instruments, data acquisition, data analysis, and manuscript preparation. PJE participated in deploying instruments to the Schenectady site, data analysis and manuscript preparation. SZE participated in data analysis and manuscript preparation. DM participated in development, construction, and deployment of the radio receiving systems, and consulted on data analysis and manuscript preparation. TK participated in development and maintenance of software for acquisition and archiving of the radio data.

Competing Interests

The authors declare that they have no conflict of interest.

Acknowledgments

The work at Dartmouth College was supported by National Science Foundation grant AGS-1915058. Total electron content data is provided to the community through Millstone Hill Geospace Facility operations at MIT Haystack Observatory under National Science Foundation grant AGS-1952737 to the Massachusetts Institute of Technology. SRZ acknowledge NSF award AGS-2149698 and NASA grant 80NSSC21K1310. The authors thank many Dartmouth undergraduate students who contributed to various stages of this project, including Rongfei Lu, Jeffrey Kim, Eric Tao, Eldred Lee, Nathan Grice, and Carter Person. The authors acknowledge the citizen science contributions of the late John S. Erickson, who provided internet and station infrastructure to this project at his Schenectady, NY residence for the crucial WGY reference clear channel station recording.

References

Beley, Vasily S., Galushko, V. G., and Yampolski, Y. M.: Traveling ionospheric disturbance diagnostics using HF signal trajectory parameter variations, Radio Science, 30, 1739-1752, 1995.

Chan, K. L., and Villard, O. G.: Observation of large-scale traveling ionospheric disturbances by spaced-path high-frequency instantaneous-frequency measurements, Journal of Geophysical Research, 67, 973-988, 1962.

Chilcote, M., LaBelle, J., Lind, F. D., Coster, A. J., Miller, E. S., Galkin, I. A., and Weatherwax, A. T.: Detection of traveling ionospheric disturbances by medium-frequency Doppler sounding using AM radio transmissions, Radio Science, 50, 249-263, 2015.

Chum, J., F. Bonomi, A. M., Fišer, J., Cabrera, M. A., Ezquer, R. G., Burešová, and D., Laštovička, J.: Propagation of gravity

535   waves and spread F in the low-latitude ionosphere over Tucumán, Argentina, by continuous Doppler sounding: First

        results, Journal of Geophysical Research: Space Physics, 119, 6954-6965, 2014.

Chum, J., and Podolska, K.: 3D Analysis of GW Propagation in the Ionosphere, Geophys. Res. Lett., 45, 11562-11571, 2021.

Cooper, Chelsey, Mitchell, C. N., Wright, C. J., Jackson, D. R., and Witvliet, B. A.: Measurement of ionospheric total electron

        content using single-frequency geostationary satellite observations, Radio Science, 54, 10-19, 2019.

540 Davis, T. N., and Sugiura, M.: Auroral electrojet activity index AE and its universal time variations, J. Geophys. Res., 71, 785–

        801, 1966.

Davies, K.: A measurement of ionospheric drifts by means of a Doppler shift technique, J. Geophys. Res., 67, 4909-4913,

        1962.

Ding, F., Wan, W., Liu, L., Afraimovich, E. L., Voeykov, S. V., and Perevalova, N. P.: A statisticalstudy of large-scale

545   traveling ionospheric disturbances observed by GPS TEC during major magnetic storms over the years 2003–

        2005, Journal of Geophysical Research: Space Physics, 113, doi:10.1029/2008JA013037, 2008.

Ding, Feng, Wan, W., Li, Q., Zhang, R., Song, Q., Ning, B., Liu, L., Zhao, B., and Xiong, B.: Comparative climatological

        study of large-scale traveling ionospheric disturbances over North America and China in 2011–2012, Journal of

        Geophysical Research: Space Physics,119, 519-529, 2014.

550 Essen, Louis: International frequency comparisons by means of standard radio frequency emissions, Proceedings of the Royal

        Society of London. Series A-Mathematical and Physical Sciences, 149, 506-510, 1935.

Fenwick, Richard C., and Villard, O. G.: Continuous recordings of the frequency variation of the WWV-20 signal after

        propagation over a 4000-km path, Journal of Geophysical Research, 65, 3249-3260, 1960.

Fišer, Jiří, Chum, Jaroslav, and Liu, Jann-Yenq: Medium-scale traveling ionospheric disturbances over Taiwan observed with

555   HF Doppler sounding, Earth, Planets and Space, 69, 1-10, 2017.

Francis, S. H.: Global propagation of atmospheric gravity waves: A review, Journal of Atmospheric and Terrestrial Physics,

        37, 1011–1054, 1975.

Frissell, Nathaniel A., Kaeppler, S. R., Sanchez, D. F., Perry, G. W., Engelke, W. D., Erickson, P. J., Coster, A. J., Ruohoniemi,

        J. M., Baker, J. B. H., and West, M. L.: First observations of large scale traveling ionospheric disturbances using

560   automated amateur radio receiving networks, Geophysical Research Letters, 49, doi:10.1029/2022GL097879, 2022.

Fritts, David C., and Alexander, M. Joan: Gravity wave dynamics and effects in the middle atmosphere, Reviews of

        Geophysics, 41, 1-68, doi:10.1029/2012RG000409, 2003.

Galushko, V. G., V. S. Beley, V. S., Koloskov, A. V., Yampolski, Yu M., Paznukhov, V. V., Reinisch, B. W., Foster, J. C.,

        and Erickson, P.: Frequency-and-angular HF sounding and ISR diagnostics of TIDs, Radio Science, 38,

565   doi:10.1029/2002RS002861, 2003..

Hernández-Pajares, M., Juan, J. M., Sanz, J., and Aragón-Àngel, A.: Propagation of medium scale traveling ionospheric

        disturbances at different latitudes and solar cycle conditions, Radio Sci., 47, doi:10.1029/2011RS004951, 2012..

Hocke, K., and Schlegel, K.: A review of atmospheric gravity waves and travelling ionospheric disturbances: 1982–1995, Annales geophysicae, 14, 917, 1996.

570 Hocking, W. K.: Performing Fourier transforms on extremely long data streams, Computers in Physics, 3, 59-65, 1989.

Hunsucker, Robert D.: Atmospheric gravity waves generated in the high-latitude ionosphere: A review, Reviews of Geophysics, 20, 293-315, 1982.

Johnson, J. B., Arechiga, R. O., Thomas, R. J., Edens, H. E., Anderson, J., and Johnson, R., Imaging thunder, Geophysical Research Letters, 38, doi:10.1029/2011GL049162, 2011.

575 Joyner, E. H., and Butcher, E. C.:Gravity wave effects in the nighttime F-region, J. Atmos. Terr. Phys., *42*, 455-459, 1980.

Kelley, M. C.: On the origin of mesoscale TIDs at midlatitudes, Annales Geophysicae, 29, 361-366, 2011.

LaBelle, J.: "Replication data for: Tracking Traveling Ionospheric Disturbances through Doppler-shifted AM radio transmissions," Harvard dataverse, https://doi.org/10.7910/DVN/L3JXIH.

Lacross, R. T., Kelly, E. J., and Toksoz, M. N.: Estimation of seismic noise structure using arrays, Geophysics, 34, 21-38, 580   1969.

Makela, J. J., and Otsuka, Y.: Overview of Nighttime Ionospheric Instabilities at Low- and Mid-Latitudes: Coupling Aspects Resulting in Structuring at the Mesoscale, Space Science Reviews, 168, 419–440, 2011.

Martinis, C., Baumgardner, J., Wroten, J., and Mendillo, M.: Seasonal dependence of MSTIDs obtained from 630.0 nm airglow imaging at Arecibo, Geophysical Research Letters, 37, doi:10.1029/2010GL043569, 2010.

585 Narayanan, V. L., Shiokawa, K., Otsuka, Y., and Neudegg, D.:On the role of thermospheric winds and sporadic E layers in the formation and evolution of electrified MSTIDs in geomagnetic conjugate regions, Journal of Geophysical Research: Space Physics, 123, 6957-6980, 2018.

Otsuka, Y., Suzuki, K., Nakagawa, S., Nishioka, M., Shiokawa, K., and and Tsugawa,T.: GPS observations of medium-scale traveling ionospheric disturbances over Europe, Annales Geophysicae, 31, 163-172, 2013.

590 Paznukhov, V. V., Galushko, V. G., and Reinisch, B. W.: Digisonde observations of TIDs with frequency and angular sounding technique, Advances in Space Research, 49, 700-710, 2012.

Perkins, Francis: Spread F and ionospheric currents, Journal of Geophysical Research, 78, 218-226, 1973.

Ransom, Scott M., Eikenberry, Stephen M., and Middleditch, John: Fourier techniques for very long astrophysical time-series analysis, The Astronomical Journal, 124, 1788, 2002.

595 Reznychenko, A. I., Koloskov, A. V., Sopin, A. O., and Yampolski, Y. O.: Statistic of Seasonal and Diurnal Variations of Doppler Frequency Shift of HF Signals at Mid-Latitude Radio Path, Radio Physics and Radio Astronomy, 25,118, 2020.

Richmond, A. D.: Gravity wave generation, propagation, and dissipation in the thermosphere, Journal of Geophysical Research: Space Physics, 83, 4131-4145, 1978.

600 Sears, R. D.: Ionospheric HF Doppler dispersion during the eclipse of 7 March 1970 and TID analysis, Journal of Atmospheric and Terrestrial Physics, 34, 727-732, 1972.

She, C.-Y., Yan, Z.-A., Gardner, C. S., Krueger, D. A., and Hu, X.: Climatology and seasonal variations of temperatures and gravity wave activities in the mesopause region above Ft. Collins, CO (40.6°N, 105.1°W), Journal of Geophysical Research: Atmospheres, 127, doi:10.1029/2021JD036291, 2022.

605 Shibata, Takashi, and Okuzawa, Takahashi: Horizontal velocity dispersion of medium-scale travelling ionospheric disturbances in the F-region, Journal of Atmospheric and Terrestrial Physics, 45, 149-159, 1983.

Shiokawa, K., Ihara, C., Otsuka, Y., and Ogawa, T.: Statistical study of nighttime medium-scale traveling ionospheric disturbances using midlatitude airglow images, Journal of Geophysical Research: Space Physics, 108, doi:10.1029/2002JA009491, 2003.

610 Song, Qian, Ding, Feng, Wan, Weixing, Ning, Baiqi, Liu, Libo, Zhao, Biqiang, Li, Qiang, and Zhang, Rui:Statistical study of large-scale traveling ionospheric disturbances generated by the solar terminator over China, Journal of Geophysical Research: Space Physics, 118, doi: 10.1002/jgra.50423, 4583-4593, 2013.

Tanaka, Teruya, Ichinose, Takumi, Okuzawa, Takashi, Shibata, Takashi, Sato, Yoshiaki, Nagasawa, Chikao, and Ogawa, Toru: HF-Doppler observations of acoustic waves excited by the Urakawa-Oki earthquake on 21 March 1982, J. Atmos.
615 Terr. Phys., 46, 233-245, 1984.

Tedd, B. L., Strangeways, H. J., and Jones, T. B.: The influence of large-scale TIDs on the bearings of geographically spaced HF transmissions, J. Atmos. Terr. Phys., 46, 109-117, 1984.

Toman, K.: On wavelike perturbations in the F region, Radio Sci., 11,107-119, 1975.

Tsugawa, T., Saito, A., and Otsuka, Y.: A statistical study of large-scale traveling ionospheric disturbances using the GPS
620 network in Japan, Journal of Geophysical Research: Space Physics, 109, doi:10.1029/2003JA010302, 2004.

Tsugawa, Takuya, Otsuka, Y., Coster, A. J., and Saito, A.: Medium-scale traveling ionospheric disturbances detected with dense and wide TEC maps over North America, Geophysical Research Letters, 34, doi:10.1029/2007GL031663, 2007.

Tsutsui, Minoru, Horikawa, Takashi, and Ogawa, Toru: Determination of velocity vectors of thermospheric wind from
625 dispersion relations of TID's observed by an HF Doppler array, J. Atmos. Terr. Phys., 46, 447-462, 1984.

Yakovets, A. F., Vodyannikov, V. V., Andreev, A. B., Gordienko, G. I., and Litvinov, Yu G.: Features of statistical distributions of large-scale traveling ionospheric disturbances over Almaty, Geomagnetism and Aeronomy, 51, 640-645, 2011.

Yeh, Kung C., and Liu, Chao H. Acoustic-gravity waves in the upper atmosphere, Reviews of Geophysics, 12, 193-216, 1974.

630 Zhang, Shun-Rong, Erickson, P. J., Goncharenko, L. P., Coster, A. J., Rideout, W., and Vierinen,J.: Ionospheric bow waves and perturbations induced by the 21 August 2017 solar eclipse, Geophysical Research Letters, 44, doi:10.1029/2017GL076054, 2017.

Zhang, Shun-Rong, Coster, A. J., Erickson, P. J., Goncharenko, L. P., Rideout, W., and Vierinen, J.: Traveling ionospheric disturbances and ionospheric perturbations associated with solar flares in September 2017, Journal of Geophysical
635 Research: Space Physics, 124, 5894-5917, 2019.Zhang, S.-R., Nishimura, Y., Erickson, P. J., Ercha, Aa, Kil, H.,

Deng, Y., Thomas, E. G., Rideout, W., Coster, A. J., Kerr, R. and Vierinen, J.: Traveling Ionospheric Disturbances in the Vicinity of Storm-Enhanced Density at Midlatitudes, Journal of Geophysical Research: Space Physics, 127, doi:10.1029/2022JA030429, 2022.